

# High Temperature Fermi Statistics from Majorana Fermions in an Insulating Magnet

Yiping Wang,<sup>1</sup> Gavin B. Osterhoudt,<sup>1</sup> Yao Tian,<sup>2</sup> Paige Lampen-Kelley,<sup>3,4</sup> Arnab Banerjee,<sup>4</sup> Thomas Goldstein,<sup>5</sup> Jun Yan<sup>5</sup>, Johannes Knolle,<sup>6</sup> Joji. Nasu,<sup>7</sup> Yukitoshi. Motome,<sup>8</sup> Stephen Nagler,<sup>4</sup> David Mandrus,<sup>3</sup> Kenneth S. Burch<sup>1</sup>

<sup>1</sup>*Department of Physics, Boston College, 140 Commonwealth Avenue, Chestnut Hill, MA 02467, USA*

<sup>2</sup>*SICK Product Center Asia Pte. Ltd., 8 Admiralty Street, Singapore 757438*

<sup>3</sup>*Department of Materials Science and Engineering, University of Tennessee, Knoxville, TN 37821, USA*

<sup>4</sup>*Materials Science and Technology Division, Oak Ridge National Laboratory, Oak Ridge, TN 37821, USA*

<sup>5</sup>*Department of Physics, University of Massachusetts, Amherst, Massachusetts 01003, USA*

<sup>6</sup>*Blackett Laboratory, Imperial College London, London SW7 2AZ, United Kingdom*

<sup>7</sup>*Department of Physics, Tokyo Institute of Technology, Meguro, Tokyo 152-8551, Japan*

<sup>8</sup>*Department of Applied Physics, University of Tokyo, Bunkyo, Tokyo 113-8656, Japan*

**Majorana fermions, particles that are their own anti-particles, can emerge in insulating magnets as excitations with fractions of the constituent's quantum numbers<sup>1-3</sup>. Interest in Majoranas is driven by their potential for quantum computation, and as evidence of novel topological states<sup>4,5</sup>. Observations have been limited to liquid helium temperatures as edge modes in**

**topological superconductors<sup>6,7</sup> and quantum spin liquids (QSL)<sup>2</sup> without combined evidence of particle-hole symmetry, Fermi statistics, and presence in the bulk. Here we report all three in  $\alpha$ -RuCl<sub>3</sub>, at temperatures exceeding liquid nitrogen via new energy gain as well as loss Raman spectra and a unique framework to identify the statistical properties of the Kitaev QSL.  $\alpha$ -RuCl<sub>3</sub> is close to the Kitaev QSL<sup>2,8-14</sup>, where bond-dependent Ising interactions produce excitations that are non-local in terms of spin flips<sup>4,5,15,16</sup>. Consistent with particle-hole symmetric excitations obeying Pauli-exclusion, the sum of the energy loss and gain responses are nearly temperature and energy independent. This is in excellent agreement with new quantum Monte Carlo (QMC) calculations of the Kitaev QSL. The new data allow unambiguous separation of the bosonic thermal fluctuations from the continuum due to the Majoranas, further establishing their presence above liquid nitrogen. Our new method can be used to identify the unique properties of QSLs, and demonstrates the promise of  $\alpha$ -RuCl<sub>3</sub> for efforts in topological phases and quantum computation.**

A key signature of long range entanglement in non-trivial topological systems are excitations with distinct exchange properties<sup>4,5,15,16</sup>. Two challenges are probing the fractional statistics, and observing them above liquid helium temperatures. Majorana fermions emerging from an abelian phase of a QSL should obey the Pauli-exclusion principle with a particle-hole symmetric density of states<sup>4,15</sup>. Here, the resulting conservation of the response is revealed in a frustrated magnet for the first time, by a temperature independent sum of our new creation and annihilation Raman spectra. The high temperature, bosonic fluctuations are also unambiguously separated from the Majoranas via a symmetry analysis. Strengthened by direct quantitative comparison with QMC calculations,

and measurements at a second wavelength, we demonstrate  $\alpha$ -RuCl<sub>3</sub> 's bulk response is consistent with the presence of Majorana fermions above liquid nitrogen temperatures.

High temperature Majoranas were proposed in relativistic Mott insulators.<sup>4,15,17,18</sup> The exact solution consists of spin-1/2 moments on a 2D honeycomb lattice with bond-dependent Ising interactions (Fig. 1a). This frustrated interaction ( $J_K$ ) hinders a static, long-range ordered ground state, but produces Majorana fermions and plaquette fluxes via fractionalization of spins<sup>4,15</sup>. Promising candidates are  $\alpha$ -RuCl<sub>3</sub> and Li<sub>2</sub>IrO<sub>3</sub><sup>8,19–23</sup>, with  $J_K \approx 100$  K though in our samples non-Kitaev terms produce zig-zag antiferromagnetism<sup>11</sup> below  $T_N \approx 7$  K (see Extended Data Fig. 1). Still elusive are direct bulk tests for the fractional statistics and particle-hole symmetry, despite evidence for Kitaev-like behavior via a continuum of magnetic excitations,<sup>2,8–12,14,17,20</sup> and half-quantized chiral edge currents<sup>2</sup>.

Dynamical scattering experiments can confirm the presence of fractional particles in QSL by probing their creation and annihilation, dictated by their kinematics and statistics.<sup>3,8,24–26</sup> Similar to asymptotic freedom in quantum chromodynamics, above the magnetic ordering temperature fractionalized excitations may dominate the short time (higher frequency) behavior of materials with a nearby QSL phase.<sup>8</sup> Raman scattering should reveal the Fermi statistics and particle-hole nature via measurement of the creation (Stokes) and annihilation (anti-Stokes) spectra. Indeed, pairs of Majorana fermions of the Kitaev QSL can be excited or absorbed (Fig. 1b)<sup>19,20,25</sup>. This is seen in our new high quality Stokes and anti-Stokes spectra (see Fig. 1c for  $T > T_N$ ), which reveal a broad continuum due to pair creation and annihilation. Furthermore, for the first time

the spectra are directly compared with new QMC calculations revealing excellent agreement at all temperatures (see supplemental). We observe equal weight in both polarization configurations, consistent with the assumption of nearly similar strength of the Kitaev interaction on the bonds<sup>19,25</sup>. The new anti-stokes spectra enables the first examination of the particle-hole symmetry, isolation of the fermionic from higher temperature bosonic fluctuations, and elimination of other continuum sources.

Raman intensity is determined by Fermi's golden rule, and via the fluctuation-dissipation theorem, related to the Raman susceptibility ( $\chi[\omega, T]$ ) times a Bose function<sup>24</sup>. In magnets this can produce peaks from one-magnons, a broad feature reflecting the two-magnon joint density of states, or quasi-elastic scattering (QES) from thermal fluctuations<sup>20,26-28</sup>. For the Kitaev QSL, Raman excites predominantly pairs of Majorana fermions in the energy range considered here ( $\approx 0.5J_K < \hbar\omega < \approx 2J_K$ ), leading to the expected energy loss ( $I_S[\omega, T]$ ) and gain ( $I_{aS}[\omega, T]$ ) intensities:

$$I_S[\omega, T] = (n_B[\omega, T] + 1)\text{Im}[\chi[\omega, T]] = (1 - n_F[\omega/2, T])^2 JDos[\omega, T]$$

$$I_{aS}[\omega, T] = (n_B[\omega, T])\text{Im}[\chi[\omega, T]] = (n_F[\omega/2, T])^2 JDos[-\omega, T]$$

where  $n_{B/F}[\omega, T]$  are the Bose/Fermi distributions and  $JDos[\omega, T]$  is approximately given by the Majorana joint density of states<sup>19</sup>.

For typical excitations governed by Bose statistics (i.e. not fractional), these are best investigated via  $\text{Im}[\chi[\omega, T]]$ <sup>24,26,28,29</sup>. Using our new anti-Stokes spectra, we directly determine the susceptibility from the difference between the Stokes and anti-Stokes intensities ( $I_S[\omega, T] -$

$I_{aS}[\omega, T] = Im[\chi[\omega, T]]$ )<sup>24</sup>. In Fig. 2a the result is plotted for surface temperatures ( $T_{Raman}$ , accounting for laser heating discussed later) up to 75 K. We observe a surprising reduction of  $Im[\chi[\omega, T]]$  upon heating the material. Since we are well above the ordering temperature, one does not expect to observe two-magnon excitations or their suppression<sup>20,24,26–28</sup>. Nonetheless, the energy and temperature scales of the suppressed  $Im[\chi[\omega, T]]$  are consistent with the Kitaev exchange energy in  $\alpha$ -RuCl<sub>3</sub><sup>8,17,19,20,22,23</sup>. Additionally, there is excellent agreement between the energy and temperature dependence of  $Im[\chi[\omega, T]]$  and the QMC calculation (Fig. 2b), providing new evidence that the continuum and its suppression upon heating results from Majorana fermions.

There should be two crucial signatures of Majorana fermions in the Raman spectra, resulting from Pauli exclusion and particle-hole symmetry. First, the intensity will shift from Stokes to anti-Stokes, as temperature moves particles from below to above the Fermi level (zero for Majoranas). Second, the Stokes and anti-Stokes response is best described by a Fermi distribution and not differences in the particle and hole density of states. To confirm these signatures, here we introduce the quantity  $I_{sum}[\omega, T] \equiv (\sqrt{I_S[\omega, T]} + \sqrt{I_{aS}[\omega, T]})^2$ . Accounting for the fact that Raman excites predominantly pairs of Majoranas in the energy range considered here, this quantity approximately extracts the joint density of states:  $I_{sum}[\omega, T] = JDos[\omega, T] + \sqrt{(n_F[\omega/2, T])}(JDos[-\omega, T] - JDos[\omega, T])^2$ , where the second term vanishes for particle-hole symmetric excitations.

We show the low temperature  $I_{sum}[\omega, T < 75 K]$  in the bottom of Fig. 2c & d, finding excellent agreement between the data and the QMC calculated response for Majorana fermions in the Kitaev QSL. Particularly, the QMC result indicates that  $JDos[\omega, T]$  hardly depends on

$\omega$  or  $T$ . This is consistent with the experimentally measured  $I_{sum}[\omega, T < 75 \text{ K}]$ , which are nearly temperature and energy independent over almost an order of magnitude of Raman shift ( $\approx 0.5J_K < \hbar\omega < \approx 2J_K$ ). We also note that the lowest temperature shown is equal to the minimum energy, yet the data continue to scale even when we raise the temperature by a factor of two. The temperature and energy independence in  $I_{sum}[\omega, T < 75 \text{ K}]$ , is exactly what we expect for fractional, fermionic particles with particle-hole symmetry; namely the intensity of the response is conserved between the energy loss and energy gain, due to particle hole symmetry and Pauli exclusion. As such, the new approach to the Raman spectra provide a second, and much stronger quantitative evidence, that the magnetic excitation in  $\alpha\text{-RuCl}_3$  are from Majorana fermions.

These are in stark contrast to the high temperature, bosonic response. Specifically, as shown in the upper part of Fig. 2c,  $I_{sum}[\omega, T > 75 \text{ K}]$  displays a low energy divergence that grows with heating due to thermal fluctuations of the magnetism (QES). These are consistent with the predicted response for Bosons (upper part of Fig. 2d), where a constant Raman susceptibility is assumed. As expected for particles without exclusion, there is no conservation of particle number and a strong enhancement of the signal results.

The upper bounds for the Majorana fermions require separating the QES, which complicated previous attempts to compare with a Fermi-Dirac distribution<sup>19,30</sup>. This is now possible using both the polarization and Stokes minus anti-Stokes spectra ( $Im[\chi[\omega, T]]$ ). Since the continuum has equal weight in both polarizations<sup>25</sup>, it can be removed via their difference:  $\Delta I_{S/aS}[\omega, T] =$

$I_{S/aS}^{XX}[\omega, T] - I_{S/aS}^{XY}[\omega, T]$ . As seen in Fig. 3a,  $\Delta I_{S/aS}[\omega, T]$  is consistent with thermal fluctuations (i.e. QES)<sup>28,29</sup>, namely a Lorentzian with greater Stokes intensity due to the Bose factor (see supplemental) and no contribution from the Fermionic continuum. Next we determined the QES amplitude via the SW of the Raman susceptibility:  $SW_{QES}[T] = \int \chi^{QES}[\omega, T]d\omega = \int (\Delta I_S[\omega, T] - \Delta I_{aS}[\omega, T])d\omega$ . Consistent with direct fits of the  $\Delta I_{S/aS}[\omega, T]$ , and robust to the limits of integration (as long as phonons are not included), we find  $SW_{QES}[T] \propto T^2$  (see Fig. 3b).

Having isolated the QES and found its temperature dependence, we determine the temperature bounds of the Fermi statistics while also confirming the particle-hole symmetry. Specifically, the difference between the Stokes and anti-Stokes SW in a given polarization ( $\Delta SW[T] = \int (I_S[\omega, T] - I_{aS}[\omega, T])d\omega$ ), which includes the integrated Fermi function from the Majorana and the QES contribution (see supplemental). As shown in Fig. 3c & d for two different regions of integration, the entire temperature dependence is well fit by a Fermi response weighted by the lowest temperature data (red) combined a  $T^2$  background term (QES). The Fermi response is equal in both polarizations, consistent with the Kitaev model<sup>25</sup>. Thus with just three parameters, one fixed by the lowest temperature, we fully fit the SW for all energy ranges, temperatures, and polarizations. If particle-hole symmetry were not obeyed, a contribution from the Fermi function squared would also be expected, but is not required. Thus the results presented in Fig. 3c,d provide an additional quantitative confirmation of the presence of Majorana fermions up to high temperatures, beyond the comparison with QMC of Fig. 1c & Fig. 2a,b and the scaling analysis of Fig. 2c,d.

Unlike previous studies<sup>19,20</sup>, our new measurements limit the possibility of laser heating to

explain the low temperature upturn and confirm the sample is in detailed balance. Specifically, thermal equilibrium requires the ratio of the Stokes to anti-Stokes intensity is a Boltzmann factor that indicates the temperature in the laser spot<sup>24,26</sup>. Fig. 4a reveals a linear relationship between  $T_{Raman}$  extracted from the ratio of the Stokes to anti-Stokes intensities (see supplemental) and the crystal temperature ( $T_{cryst}$ ). Low temperatures require the laser heating the surface by 35 K, though this cannot explain the low temperature increase in the Stokes SW. Specifically, a similar rise in anti-Stokes SW would also occur, however  $I_{aS}[\omega, T]$  continuously decreases upon lowering  $T_{cryst}$  (see supplemental). Measurements with a second crystal in a different Raman setup (Fig. 4b), revealed excellent agreement at a much longer wavelength (719 vs. 532 nm). This confirms that our data do not result from laser heating, resonant Raman<sup>24</sup>, fluorescence, or hot-electron luminescence<sup>31</sup>.

The scaling of the sum, rather than the difference of the Stokes and anti-Stokes spectra (Figs. 2a-d) provides direct evidence that the magnetic excitations in  $\alpha$ -RuCl<sub>3</sub> obey Pauli-exclusion and are particle-hole symmetric. When evaluated for the bosonic, thermal fluctuations,  $I_{sum}[\omega, T]$  is strongly temperature and energy dependent. The growth of these fluctuations as  $T^2$  is unclear and not previously identified, but may result from the finite, though nearly zero momentum response of the Kitaev QSL. The new measurement of the anti-Stokes and two different laser wavelengths eliminates a variety of other causes. This also provided unambiguous separation of the QES from the fractional contributions (Fig. 4), establishing the presence of Majorana fermions up to high temperatures (Fig. 3). Thus  $\alpha$ -RuCl<sub>3</sub> is a promising platform for efforts in topological quantum computation. Our approach can also be applied to uncover the novel excitations and distinct fea-

tures of the Majorana fermions upon entering the non-abelian phase of the Kitaev QSL as well as an array of magnetic systems, including 2D atomic crystals.

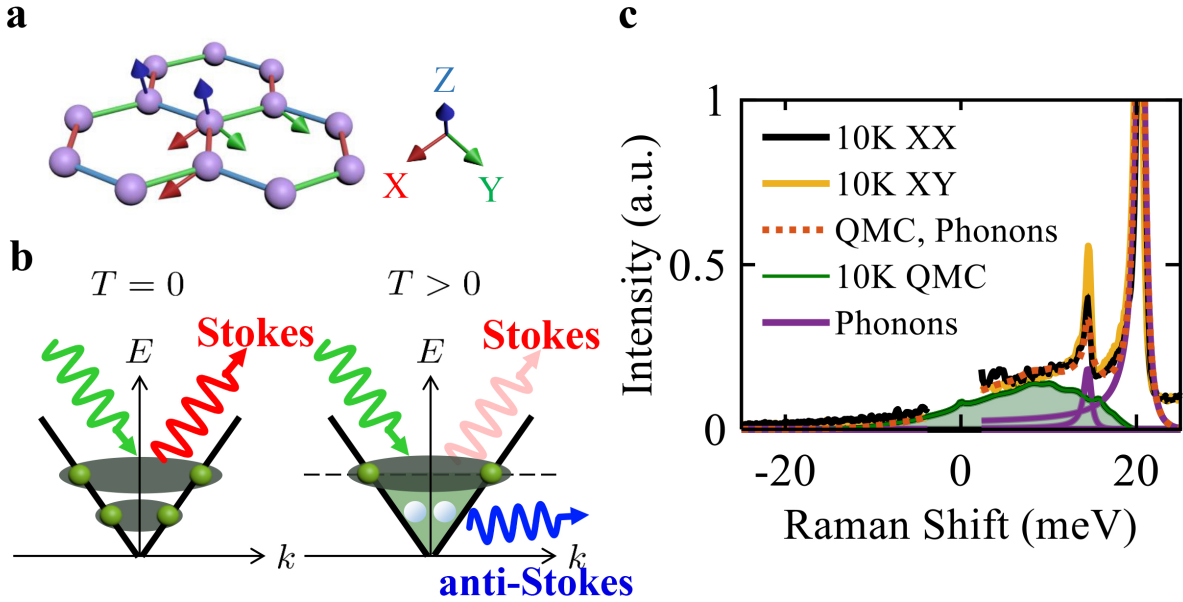


**Figure 1: Fractional Particles and Raman** (a) Bond dependent exchange of the Kitaev model. (b) For fermionic particles obeying Pauli exclusion, at zero temperature only pairs can be created giving a strong Stokes response. For higher temperatures the states become filled, enhancing anti-Stokes at the cost of Stokes. (c) Raman spectra in XX (black) and XY (yellow) polarization for the crystal at 10 K. The green area indicates the response of the fractional particles calculated from QMC including laser induced heating. Dashed red line is the fit including phonons (purple). As expected for a Kitaev system with nearly identical bonds, the continuum has equal weight in XX and XY.

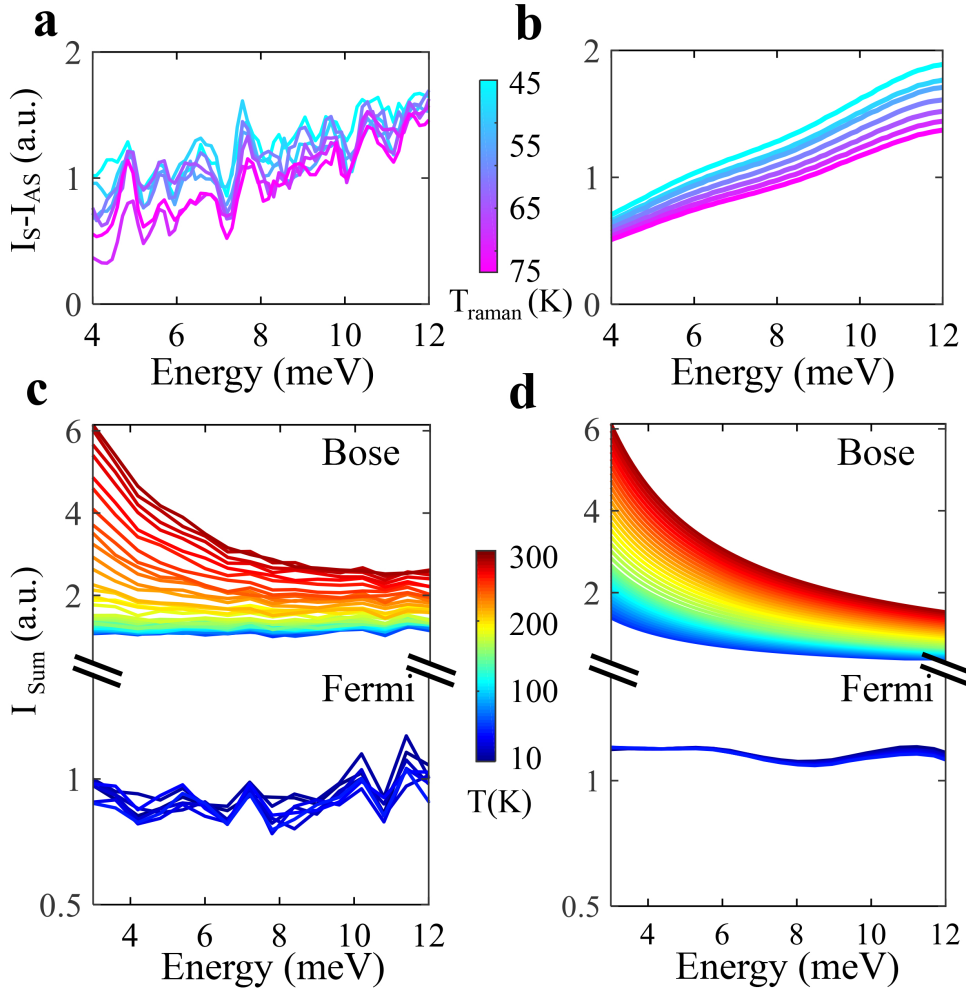


Figure 2: **Energy and Temperature Scaling** **(a-b)** Difference between the XY Stokes and anti-Stokes spectra (i.e. Raman susceptibility). The measured  $Im[\chi]$  **(a)** is reduced upon heating, matching **(b)** the QMC calculation. **(c)**  $I_{sum}$ , the sum of the loss and gain intensity, is nearly temperature independent in low temperature range ( $T < 75$  K, expanded on the bottom). This is consistent with the QMC **(d)** and results from pairs of Majorana fermions where particle-hole symmetry and Pauli-exclusion conserve the total loss and gain intensity. For the full temperature range,  $I_{sum}$  reveals an upturn from thermal fluctuations. **d** Upper axis is the same  $I_{sum}[\omega, T]$ , assuming constant  $Im[\chi[\omega, T]]$  revealing energy and temperature dependence from Bose statistics.

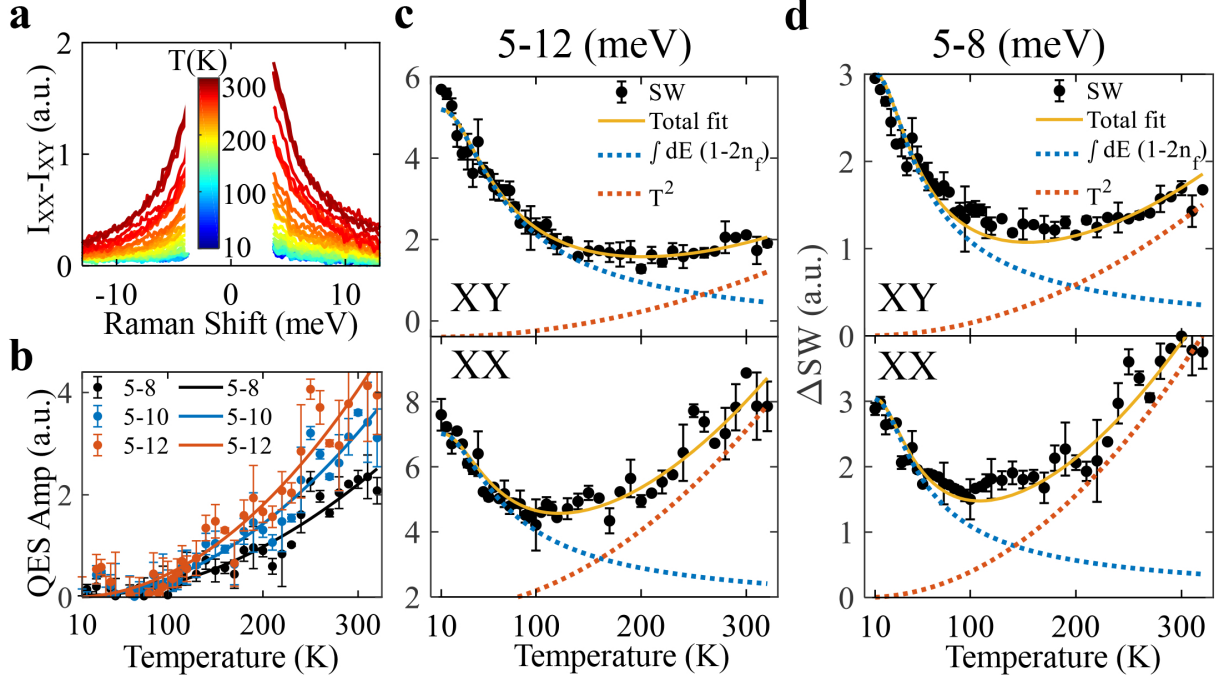
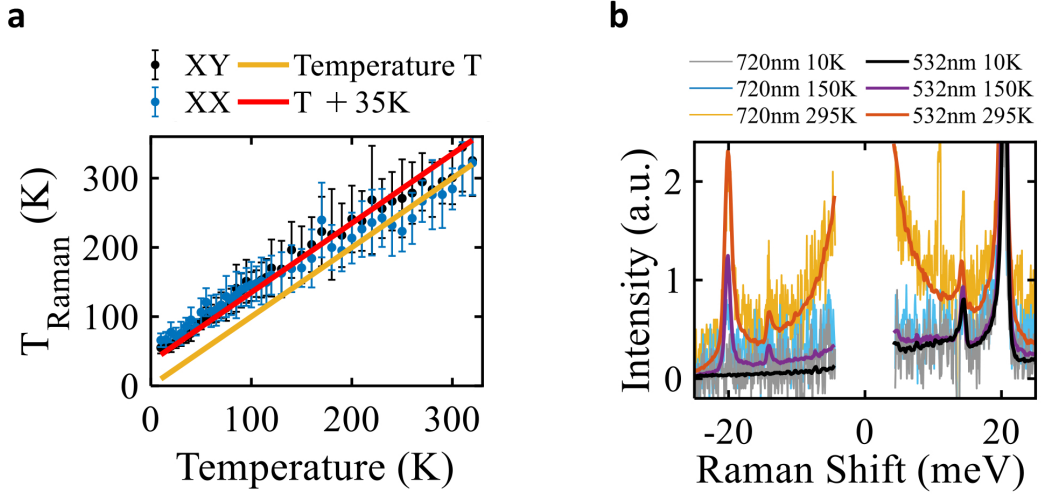


Figure 3: **Separating Bose from Fermi** **(a)** Difference between XX and XY Raman spectrum, canceling the continuum from the Majorana fermions, as expected from the Kitaev model. **(b)** Temperature dependence of the spectral weight of the Raman susceptibility for QES ( $\Delta SW_S^{XX} - \Delta SW_S^{XY}$ ), integrated across different ranges. Solid lines show fits to  $T^2$ . **(c-d)** Difference of the SW  $\Delta SW^{XY}(T) = I_S^{XY}(T) - I_{AS}^{XY}(T)$  (top panels) and  $\Delta SW^{XX}(T)$  (bottom panels) for the indicated energy ranges. A single fit of the fermionic response ( $\alpha \int (1 - 2f) d\omega$ ) is used for both symmetry channels (blue). The high temperature data is well described by the QES amplitude  $\beta T^2$  (red), with the whole range fit by the sum (yellow).



**Figure 4: Excluding heating, fluorescence and resonance** (a) Temperature of the sample determined by Raman for XX (blue) and XY (black) versus the crystal temperature. The yellow line is the assumption of perfect detailed balance, with no laser heating. The red is the response assuming the laser heats the sample by 35 K. (b) The XX Raman spectrum at 10 K, 150 K, and 295 K measured in two different systems, normalized to the phonon at 20 meV. (Green) spectra resulting from a 532 nm excitation with a single grating spectrometer and holographic notch filters. (Red) spectra from a second crystal taken with a triple grating spectrometer, nitrogen cooled detector and a 719 nm excitation. The excellent agreement confirms the continuum is not due to luminescence, resonance or an artifact of the experimental setup.

## Methods

**RuCl<sub>3</sub> crystal growth, handling and characterization.** Single crystals of  $\alpha$ -RuCl<sub>3</sub> were prepared using high-temperature vapor-transport techniques from pure  $\alpha$ -RuCl<sub>3</sub> powder with no additional transport agent. Crystals grown by an identical method have been extensively characterized via bulk and neutron scattering techniques<sup>32–34</sup> revealing behavior consistent with what is expected for a relativistic Mott insulator with a large Kiteav interaction<sup>9, 11, 13, 14, 30, 35–43</sup>. The crystals have been shown to consistently exhibit a single dominant magnetic phase at low temperature with a transition temperature  $T_N \approx 7 K$ , indicating high crystal quality with minimal stacking faults<sup>32</sup>. Care was taken in mounting the crystals to minimize the introduction of additional stacking faults, as evidenced by the high reproducibility of the spectra across different crystals and experimental setups. Characterization was consistent with previous studies<sup>10, 12, 35, 44</sup>.

**Raman spectroscopy experiments.** Since Raman scattering involves both a photon in and photon out, it allows one to measure both the symmetry and energy change of an excitation. Furthermore the photon out can be of lower or higher energy, which allows probing both the likelihood of creation and annihilation. Thus one can choose energy and/or symmetry channel to separate the magnetic, electronic and lattice responses<sup>19, 20, 24, 24, 27–29, 45–49</sup>. The majority of the Raman experiments were performed with a custom built low temperature, microscopy setup<sup>50</sup>. A 532 nm excitation laser, whose spot radius is  $0.5 \mu m$ , with power kept to  $30 \mu W$  in front of the high vacuum chamber was used to minimize heating while allowing for a strong enough signal. The sample was mounted by thermal epoxy onto an *xyz* stage. At both room and base temperature the reported spectra were averaged from three spectrum in the same environment to ensure reproducibility. The

spectrometer had a 2400 g/mm grating, with an Andor CCD, providing a resolution of  $\approx 1 \text{ cm}^{-1}$ . To minimize the effects of hysteresis from the crystal structural transition, data was taken by first cooling the crystal to base temperature and once cooled to the base temperature, spectra were acquired either every 5 K or 10 K by directly heating to that temperature. The absence of hysteresis effects were confirmed by taking numerous spectra at the same temperature after different thermal cycles (100 K in the middle of the hysteresis region). In addition, recent studies of the Raman spectra of  $\text{RuCl}_3$  suggest an effect of the surface structure upon exposure to air<sup>51,52</sup>. To minimize this, crystals were freshly cleaved and immediately placed in vacuum within five minutes. Moreover, a recently developed wavelet based approach was employed to remove cosmic rays<sup>53</sup>.

**Quantum Monte Carlo Calculations.** The Hamiltonian of the Kitaev model on the honeycomb lattice is given by

$$\mathcal{H} = -J_x \sum_{\langle jk \rangle_x} S_j^x S_k^x - J_y \sum_{\langle jk \rangle_y} S_j^y S_k^y - J_z \sum_{\langle jk \rangle_z} S_j^z S_k^z, \quad (1)$$

where  $S_j$  represents an  $S = 1/2$  spin on site  $j$ , and  $\langle jk \rangle_\gamma$  stands for a nearest-neighbor (NN)  $\gamma (= x, y, z)$  bond shown in Fig. 1a. In the calculation for the spectrum of the Raman scattering we adopt the Loudon-Fleury (LF) approach. The LF operator for the Kitaev model is given by

$$\mathcal{R} = \sum_{\langle ij \rangle_\alpha} (\epsilon_{\text{in}} \cdot \mathbf{d}^\alpha) (\epsilon_{\text{out}} \cdot \mathbf{d}^\alpha) J_\alpha S_i^\alpha S_j^\alpha, \quad (2)$$

where  $\epsilon_{\text{in}}$  and  $\epsilon_{\text{out}}$  are the polarization vectors of the incoming and outgoing photons and  $\mathbf{d}^\alpha$  is the vector connecting a NN  $\alpha$  bond<sup>25,54</sup>. Using this LF operator, the Raman spectrum is calculated as

$$I(\omega) = \frac{1}{N} \int_{-\infty}^{\infty} dt e^{i\omega t} \langle \mathcal{R}(t) \mathcal{R} \rangle, \quad (3)$$

where  $\mathcal{R}(t) = e^{i\mathcal{H}t} \mathcal{R} e^{-i\mathcal{H}t}$  is the Heisenberg representation. The temperature dependence of  $I(\omega)$

is numerically evaluated using the Monte Carlo simulation in the Majorana fermion representation without any approximation<sup>55</sup>. In the following we show the detail of the calculation procedure<sup>19</sup>.

Using the Jordan-Wigner transformation, the Hamiltonian is mapped onto the Majorana fermion model as

$$\mathcal{H} = \frac{iJ_x}{4} \sum_{(jj')_x} c_j c_k - \frac{iJ_y}{4} \sum_{(jj')_y} c_j c_k - \frac{iJ_z}{4} \sum_{(jj')_z} \eta_r c_j c_k, \quad (4)$$

where  $(jj')_\gamma$  is the NN pair satisfying  $j < j'$  on the  $\gamma$  bond, and  $\eta_r$  is a  $Z_2$  conserved quantity defined on the  $z$  bond ( $r$  is the label for the bond), which takes  $\pm 1$ . This Hamiltonian is simply written as

$$\mathcal{H} = \frac{1}{2} \sum_{jk} A_{jk}(\{\eta_r\}) c_j c_k, \quad (5)$$

using the Hermitian matrix  $A_{jk}(\{\eta_r\})$  depending on the configuration of  $\{\eta_r\}$ . The LF operator shown in Eq. (2) is also given by the bilinear form of the Majorana fermion:

$$\mathcal{R}(\{\eta_r\}) = \frac{1}{2} \sum_{jk} B_{jk}(\{\eta_r\}) c_j c_k, \quad (6)$$

where  $B(\{\eta_r\})$  is a Hermitian matrix. To evaluate Eq. (3), we separate the sum over the states into  $\{c_j\}$  and  $\{\eta_r\}$  parts:

$$I(\omega) = \frac{1}{Z} \sum_{\{\eta_r=\pm 1\}} \bar{I}(\omega; \{\eta_r\}) e^{-\beta F_f(\{\eta_r\})}, \quad (7)$$

with

$$\bar{I}(\omega; \{\eta_r\}) = \frac{1}{Z_f(\{\eta_r\})} \text{Tr}_{\{c_j\}} \left[ \frac{1}{N} \int_{-\infty}^{\infty} dt e^{i\omega t} \mathcal{R}(t; \{\eta_r\}) \mathcal{R}(\{\eta_r\}) e^{-\beta \mathcal{H}(\{\eta_r\})} \right], \quad (8)$$

where  $Z = \sum_{\{\eta_r=\pm 1\}} e^{-\beta F_f(\{\eta_r\})}$  and  $Z_f(\{\eta_r\}) = e^{-\beta F_f(\{\eta_r\})} = \text{Tr}_{\{c_j\}} e^{-\beta \mathcal{H}(\{\eta_r\})}$ . By applying Wick's theorem to Eq. (8), we calculate the Raman spectrum at  $\omega(\neq 0)$  for a given configuration

$\{\eta_r\}$  as

$$\begin{aligned}\bar{I}(\omega; \{\eta_r\}) = & \frac{1}{N} \sum_{\lambda\lambda'} \left[ 2\pi |C_{\lambda\lambda'}|^2 f(\varepsilon_\lambda) [1 - f(\varepsilon_{\lambda'})] \delta(\omega + \varepsilon_\lambda - \varepsilon_{\lambda'}) \right. \\ & + \pi |D_{\lambda\lambda'}|^2 [1 - f(\varepsilon_\lambda)] [1 - f(\varepsilon_{\lambda'})] \delta(\omega - \varepsilon_\lambda - \varepsilon_{\lambda'}) \\ & \left. + \pi |D_{\lambda\lambda'}|^2 f(\varepsilon_\lambda) f(\varepsilon_{\lambda'}) \delta(\omega + \varepsilon_\lambda + \varepsilon_{\lambda'}) \right],\end{aligned}\quad (9)$$

where  $f(\varepsilon) = 1/(1 + e^{\beta\varepsilon})$  is the Fermi distribution function with zero chemical potential,  $\{\varepsilon_\lambda\}$  is the set of the positive eigenvalues of  $A$  with the eigenvectors  $\{\mathbf{u}_\lambda\}$ , and the matrices  $C$  and  $D$  are given by  $C_{\lambda\lambda'} = 2\mathbf{u}_\lambda^\dagger B \mathbf{u}_{\lambda'}$  and  $D_{\lambda\lambda'} = 2\mathbf{u}_\lambda^\dagger B \mathbf{u}_{\lambda'}^*$ . In the Monte Carlo simulations, we generate a sequence of configurations of  $\{\eta_r\}$  to reproduce the distribution of  $e^{-\beta F_f(\{\eta_r\})}$ , and hence the finite-temperature spectrum is simply computed as  $I(\omega) = \langle \bar{I}(\omega; \{\eta_r\}) \rangle_{\text{MC}}$  with  $\langle \dots \rangle_{\text{MC}}$  being the Monte Carlo average.

**Correction for optical constants.** According to the Beer-Lambert Law, the intensity of the laser decreases exponentially with the depth:  $I[z] = I_0 e^{-\alpha z}$ , where  $d$  is the depth and  $\alpha$  is attenuation constant, which is a function of laser frequency and dielectric constant of the material ( $\alpha = \frac{\omega}{c} \text{Im}[\tilde{n}(\omega)] = -\frac{4\pi E[\omega_0]}{hc} k[\omega_0]$ ). Alternatively one can express this in terms of a penetration depth indicating the length scale relevant to absorption:  $\delta = \frac{1}{\alpha}$ . Applying this to our experiment, for a certain depth  $d$ , we find the incident laser intensity as a function of distance from the surface,  $I_{in}[\omega_0, z] = I_0 e^{-\frac{4\pi E[\omega_0]}{hc} k[\omega_0] z}$ . Here,  $\omega_0$  is the frequency of the excitation laser,  $I_0$  is the initial incoming laser power in front of the sample, and  $\delta(\approx 140 \text{ nm})$  is much shorter than the thickness of  $\alpha\text{-RuCl}_3$  bulk crystal. To properly account for the temperature dependence of the optical constants on the measured Raman signal, it is crucial to account for these absorption losses.

Specifically the measured intensity is reduced by the absorption of the outgoing Raman photons, (i.e.  $I_{out}[\omega, \omega_0, z] = I_{in}[\omega_0, z]e^{-\frac{4\pi E[\omega]}{hc}k[\omega]z}$ ) where  $\omega$  is the frequency of the scattered light. Furthermore, one should also consider the probability of transmission at the surface of  $\alpha$ -RuCl<sub>3</sub> ( $T[\omega]$ ), which also depends on the Raman light frequency. Applying the transmission rate to the Raman signal, we obtain the Raman intensity coming out of the sample at each point  $I_{Raman}[\omega, \omega_0, z] = I_{out}[\omega, \omega_0, z] * T[\omega]$ . Finally, one obtains the signal intensity by integrating the attenuated intensity of scattering point at each depth via  $I_{corrected}[\omega_0, \omega] = \int_0^{d_{max}} I_{Raman}[\omega, \omega_0, z]dz^{50,56,57}$ . All presented Raman data in this paper are corrected by this method using the previously published optical constants<sup>58</sup>.

**Acknowledgements** We are grateful for numerous discussions with Natalia Perkins, Joshua Heath, Kevin Bedell and Ying Ran. The Raman experiments at 532 nm were performed by Y.W. with support from the National Science Foundation, Award No. DMR-1709987. G.O. assisted in the analysis with support from the U.S. Department of Energy (DOE), Office of Science, Office of Basic Energy Sciences under Award No. DE-SC0018675. Raman experiments performed at 720 nm (T.G. and J.Y.) were achieved by support from the National Science Foundation, Award No. ECCS 1509599. The crystal growth and characterization (P.L.K., A.B., D.M. and S.N.) with . The numerical simulations were performed by J.N. with support from Grants-in-Aid for Scientific Research (KAKENHI) (numbers JP15K13533, JP16H02206, JP16K17747, and JP18H04223). Parts of the numerical calculations were performed in the supercomputing systems in ISSP, the University of Tokyo.

**Competing Interests** The authors declare that they have no competing financial interests.

**Author Contributions** Y.W. performed the Raman experiments, with assistance from G.O., T.G., and J.Y. Analysis was done by Y.W., J.N., J.K., and G.O. The crystal growth and initial characterization were done by P.L., A.B., and D.M. The design of the experiments and conception of the study were achieved by K.S.B., S.N. and J.K. The theoretical calculations were performed by J.N., J.K. and Y.M.

**Correspondence** Correspondence and requests for materials should be addressed to K.S. Burch (email: ks.burch@bc.edu).

1. Banerjee, M. *et al.* Observation of half-integer thermal hall conductance. *Nature* **559**, 205–210 (2018).
2. Kasahara, Y. *et al.* Majorana quantization and half-integer thermal quantum hall effect in a kitaev spin liquid. *Nature* **559**, 227–231 (2018).
3. Han, T.-H. *et al.* Fractionalized excitations in the spin-liquid state of a kagome-lattice antiferromagnet. *Nature* **492**, 406–410 (2012).
4. Kitaev, A. Anyons in an exactly solved model and beyond. *Annals of Physics* **321**, 2–111 (2006). 0506438.
5. Wen, X.-G. Zoo of quantum-topological phases of matter. *Rev. Mod. Phys.* **89**, 1–17 (2016). 1610.03911.
6. He, Q. L. *et al.* Chiral majorana fermion modes in a quantum anomalous hall insulator–superconductor structure. *Science* **357**, 294–299 (2017).

7. Mourik, V. *et al.* Signatures of Majorana Fermions in Hybrid Superconductor-Semiconductor Nanowire Devices. *Science* **336**, 1003 (2012).
8. Banerjee, A. *et al.* Proximate Kitaev quantum spin liquid behaviour in a honeycomb magnet. *Nature Materials* **15**, 733–740 (2016). 1504.08037.
9. Koitzsch, A. *et al.* J- $\{\text{eff}\}$  Description of the Honeycomb Mott Insulator  $\alpha$ -RuCl- $\{3\}$ . *Phys. Rev. Lett.* **117**, 126403 (2016).
10. Wang, Z. *et al.* Magnetic Excitations and Continuum of a Possibly Field-Induced Quantum Spin Liquid in  $\alpha$ -RuCl<sub>3</sub>. *Phys. Rev. Lett.* **119**, 227202 (2017).
11. Winter, S. M. *et al.* Breakdown of magnons in a strongly spin-orbital coupled magnet. *Nat. Commun.* **8**, 1152 (2017). 1702.08466.
12. Zheng, J. *et al.* Gapless Spin Excitations in the Field Induced Quantum Spin Liquid Phase of  $\alpha$ -RuCl<sub>3</sub>. *Phys. Rev. Lett.* **119**, 227208 (2017). 1706.06157.
13. Wellm, C. *et al.* Signatures of low-energy fractionalized excitations in  $\alpha$ -RuCl<sub>3</sub> from field-dependent microwave absorption. *arXiv preprint arXiv:1710.00670* (2017).
14. Do, S. H. *et al.* Majorana fermions in the Kitaev quantum spin system  $\alpha$ -RuCl 3. *Nat. Phys.* **13**, 1079–1084 (2017).
15. Matern, S. & Hermanns, M. Entanglement in 3d kitaev spin liquids. *Journal of Statistical Mechanics: Theory and Experiment* **2018**, 063101 (2018).

16. Savary, L. & Balents, L. Quantum spin liquids: a review. *Reports on progress in physics. Physical Society (Great Britain)* **80**, 016502 (2017). 1601.03742.
17. Catuneanu, A., Yamaji, Y., Wachtel, G., Kim, Y. B. & Kee, H.-Y. Path to stable quantum spin liquids in spin-orbit coupled correlated materials. *npj Quantum Materials* **3**, 23 (2018).
18. Jackeli, G. & Khaliullin, G. Mott Insulators in the Strong Spin-Orbit Coupling Limit: From Heisenberg to a Quantum Compass and Kitaev Models. *Physical Review Letters* **102**, 2–5 (2008). 0809.4658.
19. Nasu, J., Knolle, J., Kovrizhin, D. L., Motome, Y. & Moessner, R. Fermionic response from fractionalization in an insulating two-dimensional magnet. *Nature Physics* **12**, 912–915 (2016). 1602.05277.
20. Sandilands, L. J., Tian, Y., Plumb, K. W., Kim, Y. J. & Burch, K. S. Scattering Continuum and Possible Fractionalized Excitations in  $\alpha$ -RuCl<sub>3</sub>. *Physical Review Letters* **114** (2015). 1504.05202.
21. Modic, K. *et al.* Realization of a three-dimensional spin–anisotropic harmonic honeycomb iridate. *Nature communications* **5**, 4203 (2014).
22. Kitagawa, K. *et al.* A spin-orbital-entangled quantum liquid on a honeycomb lattice. *Nature* **554**, 341–345 (2018).
23. Majumder, M. *et al.* Breakdown of Magnetic Order in the Pressurized Kitaev Iridate  $\beta$ -Li<sub>2</sub>IrO<sub>3</sub>. *Phys. Rev. Lett.* **120**, 237202 (2018).

24. Devreux, T. P. & Hackl, R. Inelastic light scattering from correlated electrons. *Reviews of Modern Physics* **79**, 175 (2007).

25. Knolle, J., Chern, G.-W., Kovrizhin, D., Moessner, R. & Perkins, N. Raman scattering signatures of kitaev spin liquids in a 2 iro 3 iridates with a= na or li. *Physical review letters* **113**, 187201 (2014).

26. Misochko, O., Tajima, S., Urano, C., Eisaki, H. & Uchida, S. Raman-scattering evidence for free spinons in the one-dimensional spin-1/2 chains ofC and SrC. *Phys. Rev. B - Condens. Matter Mater. Phys.* **53**, R14733–R14736 (1996).

27. Kuroe, H. *et al.* Spin fluctuations in cu<sub>2</sub>ge<sub>3</sub> probed by light scattering. *Phys. Rev. B* **55**, 409–415 (1997).

28. Wulferding, D. *et al.* Interplay of thermal and quantum spin fluctuations in the kagome lattice compound herbertsmithite. *Phys. Rev. B* **82**, 144412 (2010).

29. Nakamura, Y., Kato, R. & Kishida, H. Study of Magnetic Excitation in Pd(dmit)<sub>2</sub> Salts by Raman Scattering Spectroscopy. *J. Phys. Soc. Japan* **84**, 44715 (2015).

30. Sandilands, L. J. *et al.* Spin-orbit excitations and electronic structure of the putative Kitaev magnet  $\alpha$ -RuCl<sub>3</sub>. *Phys. Rev. B* **93**, 075144 (2016).

31. Sapega, V. F., Moreno, M., Ramsteiner, M., Däweritz, L. & Ploog, K. H. Polarization of Valence Band Holes in the (Ga,Mn)As Diluted Magnetic Semiconductor. *Phys. Rev. Lett.* **94**, 137401 (2005).

32. Cao, H. B. *et al.* Low-temperature crystal and magnetic structure of  $\alpha$ -RuCl<sub>3</sub>. *Physical Review B* **93**, 134423 (2016).

33. Banerjee, A. *et al.* Neutron tomography of magnetic Majorana fermions in a proximate quantum spin liquid. *Science* **356**, 1055–1059 (2016). 1609.00103.

34. Banerjee, A. *et al.* Excitations in the field-induced quantum spin liquid state of  $\alpha$ -RuCl<sub>3</sub>. *npj Quantum Materials* **3**, 8 (2018). 1706.07003.

35. Plumb, K. W. *et al.*  $\alpha$ -RuCl<sub>3</sub>:A spin-orbit assisted Mott insulator on a honeycomb lattice. *Phys. Rev. B* **90**, 041112 (2014).

36. Becker, M., Hermanns, M., Bauer, B., Garst, M. & Trebst, S. Spin-orbit physics of  $j = \frac{1}{2}$  mott insulators on the triangular lattice. *Phys. Rev. B* **91**, 155135 (2015).

37. Zhou, X. *et al.* Angle-resolved photoemission study of the Kitaev candidate  $\alpha$ -RuCl<sub>3</sub>. *Phys. Rev. B* **94**, 161106 (2016).

38. Yadav, R. *et al.* Kitaev exchange and field-induced quantum spin-liquid states in honeycomb  $\alpha$ -RuCl<sub>3</sub>. *Scientific reports* **6**, 37925 (2016).

39. Hirobe, D., Sato, M., Shiomi, Y., Tanaka, H. & Saitoh, E. Magnetic thermal conductivity far above the Néel temperature in the Kitaev-magnet candidate  $\alpha$ -RuCl<sub>3</sub>. *Phys. Rev. B* **95**, 241112 (2017). 1611.04799.

40. Little, A. *et al.* Antiferromagnetic Resonance and Terahertz Continuum in  $\alpha$ -RuCl<sub>3</sub>. *Phys. Rev. Lett.* **119**, 227201 (2017). 1704.07357.

41. Janša, N. *et al.* Observation of two types of fractional excitation in the Kitaev honeycomb magnet. *Nature Physics* 1–5 (2018). 1706.08455.

42. Kim, H.-S. & Kee, H.-Y. Crystal structure and magnetism in  $\alpha$  – rucl<sub>3</sub>: An ab initio study. *Phys. Rev. B* **93**, 155143 (2016).

43. Leahy, I. A. *et al.* Anomalous Thermal Conductivity and Magnetic Torque Response in the Honeycomb Magnet  $\alpha$ -RuCl<sub>3</sub>. *Physical Review Letters* **118**, 187203 (2017).

44. Majumder, M. *et al.* Anisotropic Ru<sup>3+</sup> 4d<sup>5</sup> magnetism in the  $\alpha$ -RuCl<sub>3</sub> honeycomb system: Susceptibility, specific heat, and zero-field NMR. *Phys. Rev. B* **91**, 180401 (2015).

45. Gretarsson, H. *et al.* Two-magnon raman scattering and pseudospin-lattice interactions in sr<sub>2</sub>iro<sub>4</sub> and sr<sub>3</sub>ir<sub>2</sub>o<sub>7</sub>. *Phys. Rev. Lett.* **116**, 136401 (2016).

46. Blumberg, G., Kang, M., Klein, M., Kadowaki, K. & Kendziora, C. Evolution of magnetic and superconducting fluctuations with doping of high-T-c superconductors. *Science* **278**, 1427–1432 (1997).

47. Tian, Y., Gray, M. J., Ji, H., Cava, R. J. & Burch, K. S. Magneto-elastic coupling in a potential ferromagnetic 2d atomic crystal. *2D Materials* **3**, 025035 (2016).

48. Butcher, P. N. & Ogg, N. R. Fluctuation-dissipation theorems for driven non-linear media at optical frequencies. *Proceedings of the Physical Society* **86**, 699–708 (1965).

49. Glamazda, A., Lemmens, P., Do, S.-H., Kwon, Y. S. & Choi, K.-Y. Relation between Kitaev magnetism and structure in  $\alpha$ -RuCl<sub>3</sub>. *Phys. Rev. B* **95**, 174429 (2017).

50. Tian, Y. *et al.* Low vibration high numerical aperture automated variable temperature Raman microscope. *Rev. Sci. Inst.* **87**, 043105 (2016).

51. Zhou, B. *et al.* Possible structural transformation and enhanced magnetic fluctuations in exfoliated  $\alpha$ -RuCl<sub>3</sub>. *Journal of Physics and Chemistry of Solids* – (2018).

52. Mashhadi, S. *et al.* Electrical transport signature of the magnetic fluctuation-structure relation in  $\alpha$ -rucl3 nanoflakes. *Nano letters* **18**, 3203–3208 (2018).

53. Tian, Y. & Burch, K. S. Automatic spike removal algorithm for raman spectra. *Applied Spectroscopy* (2016).

54. Fleury, P. & Loudon, R. Scattering of light by one-and two-magnon excitations. *Physical Review* **166**, 514 (1968).

55. Nasu, J., Udagawa, M. & Motome, Y. Vaporization of kitaev spin liquids. *Physical Review Letters* **113**, 1–5 (2014). 1406.5415.

56. Osterhoudt, G. B. *et al.* Charge transfer in EuS/Bi<sub>2</sub>Se<sub>3</sub> heterostructures as indicated by the absence of Raman scattering. *Phys. Rev. B* **98**, 014308 (2018).

57. Yoon, D. *et al.* Interference effect on Raman spectrum of graphene on SiO<sub>2</sub>/Si. *Physical Review B* **80**, 125422 (2009).

58. Sandilands, L. J. *et al.* Optical probe of heisenberg-kitaev magnetism in  $\alpha$ - rucl 3. *Physical Review B* **94**, 195156 (2016).